NUMERICAL AND ANALYTICAL MODELING OF PRESSURE DROP THROUGH A GEOTHERMAL TWO-PHASE ORIFICE PLATE

Mohamad Husni Mubarok[1,2]*, Sadiq J. Zarrouk[1] and John E. Cater[1]

[1] Department of Engineering Science, The University of Auckland, Private Bag 92019, Auckland, New Zealand

[2] Operation and Engineering, PT. Pertamina Geothermal Energy, Jakarta, 10340, Indonesia

*mmub714@aucklanduni.ac.nz; husnimubarok@pertamina.com

Keywords: *Geothermal; Two-phase; Orifice plates; Net pressure drop; Computational fluid dynamics.*

ABSTRACT

Measurement of the total mass flow rate of two-phase (steam and brine) geothermal fluid using sharp-edge orifice plates is gaining wide acceptance by the geothermal industry. Computational fluid dynamics (CFD) simulations using the ANSYS™ Fluent software were tested and validated with pressure drop data from the field experiments in Ulubelu, Sibayak, Lahendong and Bukit Daun geothermal fields, Indonesia. A mixture method was used to simulate the combination of steam and liquid in the geothermal flows. The selection of appropriate numerical methods is discussed in detail along with the results of the simulations including pressure, velocity and discharge coefficients. A new analytical correlation to predict the net pressure drop and mass flow rate is proposed and compared with the CFD models and the field test data. Good agreement has been observed between CFD predictions, the proposed correlation and the experimental data for net pressure drop across the orifice plate. This should help when sizing a suitable orifice plate at minimum pressure drop in future implementation.

NOMENCLATURE

A	Pipe area (m^2)
AC	Acceleration correction factor
C	Orifice discharge coefficient
C_c	Contraction coefficient
CFD	Computational fluid dynamics
Co	Courant number
D	Inside pipe diameter (m)
d	Orifice diameter (m)
E	Orifice plate thickness (mm)
e	Sharp-edge orifice plate thickness (mm)
f	Friction factor
G	Mass flux (kg/s.m^2)
h	Enthalpy (kJ/kg)
k	Turbulent kinetic energy (m^2/s^2)
K	Parameter in equation (12 and 14)
L	Pipe length (m)
$\dot{m}$	Mass flow rate of the fluid (kg/s)
p_1	Pressure upstream of the orifice plate (Pa)
p_2	Pressure downstream of the orifice plate (Pa)
$RANS$	Reynolds average Navier Stokes
Re	Reynolds number
u	Fluid velocity (m/s)
v	Specific volume (m^3/kg)
x	Dryness fraction of the fluid
Greek letters	
σ	Area ratio
β	Ratio of the orifice diameter to the inside pipe diameter ($\beta = d/D$)
μ	Dynamic viscosity (kg/ms)
ρ	Density (kg/m^3)
Δp	Differential pressure (Pa)
τ	Wall shear stress (Pa/m)
ω	Specific dissipation rate (1/s)
ϕ	Parameter in equation (15)
Subscripts	
C	Contraction
e	Effective
f	Frictional
g	Gravitational
G	Gaseous/steam phase
L	Liquid phase
m	Momentum
seg	Segment
TP	Two-phase

1. INTRODUCTION

The sharp edge orifice plate can be used to measure the mass flow rate of single and two-phase geothermal fluid with a host of two-phase flow correlations have been used by the industry (Helbig and Zarrouk, 2012). A new correlation by Mubarok, et al., (2017) has been used to calculate two-phase flow rate with high accuracy for a wide range of geothermal reservoir enthalpies (600 to 2800 kJ/kg).

The pressure drop of geothermal two-phase fluid increases close to the orifice because the restriction produces higher velocity. The pressure decline rate reduce after the orifice to fully developed conditions. The total pressure drop is called the "net pressure drop". Low net pressure drop is desirable for geothermal applications to minimize the total pressure drop in the two-phase geothermal pipeline systems. Currently, there are no specific methods to determine the net

pressure drop. A new pressure drop correlation was developed that can be used to predict the net pressure drop across the orifice plate, which was validated using numerical flow modeling through computational fluid dynamics (CFD).

Computational fluid dynamics (CFD) is the use of computer numerical modeling to derive fluid flow behavior (Versteeg & Malalasekera, 1995). CFD is used to make predictions for fluid flow in a certain system at a specified conditions. The results of CFD flow solutions are also more comprehensive than many experimental methods, which are limited by the availability, precision and accuracy of measuring instruments. In general, there are three steps in CFD numerical modeling; a pre-processor, solver and a post-processor. Each of the steps contributes to the quality of the simulation results, thus the parameters have to be considered carefully at every step in order to minimize error.

Some studies in geothermal applications have been done using CFD simulation; for example failure analysis (Fadli, Karim, Harahap, & Taufik, 2015; Mazur, Garcia-Illescas, & Porcayo-Calderon, 2009), two-phase flow in a separator vessel (Pointon, Mills, Seil, & Zhang, 2009; Purnanto, Zarrouk, & Cater, 2012; Zarrouk & Purnanto, 2014), wellbore or pipeline flow (Deendarlianto et al., 2016; Osato, Sato, & Kasai, 2016) and orifice plate flow (Hollingshead, 2011; Jithish & Kumar, 2015; Roul & Dash, 2012; Shah, Joshi, Kalsi, Prasad, & Shukla, 2012; Siba, Mahmood, Nuawi, Rasani, & Nassir, 2015; Urner, 1997; Zahariea, 2016).

Most of the previous work has been concentrated on CFD modeling orifice plate and pipe flow of non-geothermal fluids. Previous work that used CFD modeling of geothermal fluid flow by Pointon et al. (2009) and Zarrouk and Purnanto (2014). However, these studies covered geothermal fluid behavior inside a cyclone separator.

This work deals with the prediction of the upstream and downstream pressure difference of a sharp-edge orifice plate in a geothermal two-phase pipeline using analytical and numerical approaches. A predicted downstream pressure from a proposed correlation and CFD simulation were validated with pressure gauge monitoring data from geothermal wells (UBL-K/3, SBY-3, LHD-37/2 and BDN-A/1). Predicting the pressure drop is useful for calculating: the discharge coefficient ($C_{L/G}$), fluid pressure, velocity profile distribution inside the pipeline, which is important for calculating the mass flow rate.

2. NET PRESSURE DROP

The net pressure drop (Δp_{net}) of two-phase fluid in a straight pipeline is the sum of three components: frictional (Δp_f), gravitational (Δp_g) and acceleration/momentum (Δp_m). The net pressure drop can therefore be expressed as:

$$\Delta p_{net} = \Delta p_f + \Delta p_g + \Delta p_m. \quad (1)$$

In a horizontal pipe, the gravitational pressure drop component (Δp_g) can be neglected since there is no change in elevation. The predicted net pressure drop through an orifice plate in horizontal pipe can be calculated in three separate segments (Figure 1). The first and third segment can be represented by frictional pressure drop alone. While the pressure drop in the second segment (across the orifice plate) is a combination of the momentum (Δp_m) and the contraction (Δp_C) pressure drop. The contraction pressure drop occurs due to the sudden contraction caused by the orifice plate in the pipe.

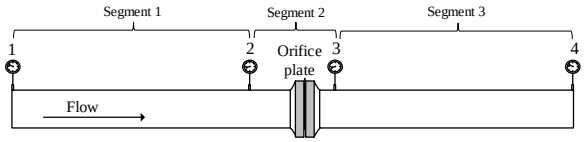

Figure 1: Pipe segmentation to calculate net pressure drop of orifice plate.

2.1 Frictional Pressure Drop

To predict the friction pressure drop in the pipeline, the correlation from Freeston (1980) was used. This correlation has been applied in two-phase geothermal pipeline designs for small and large pipe size diameters. The Freeston (1980) method was specified for the annular flow regime and a wide flow rate range. The friction pressure drop can be written as:

$$\Delta p_f = \frac{4\tau_L L}{D(1-AC)}. \quad (2)$$

The wall shear stress (τ_L) and the dimensionless correction factor (AC) are calculated using the following equations:

$$\tau_L = f\frac{\rho_L {V_L}^2}{8}, \quad (3)$$

$$AC = \frac{\dot{m}^2 x^2}{\alpha A^2 \rho_G P}. \quad (4)$$

To use the correlations (3) and (4), the liquid superficial velocity (V_L) and void fraction (α) can be calculated by:

$$V_L = \frac{\dot{m}_L}{\rho_L A(1-\alpha)}, \quad (5)$$

$$\alpha = \frac{1}{1+\left(\frac{1-x}{x}\right)^{0.8}\left(\frac{\rho_g}{\rho_l}\right)^{0.515}}. \quad (6)$$

The friction factor (f) is calculated using the Churchill correlation (Mundakir, 2001):

$$f = 8\left(\left(\frac{8}{Re}\right)^{12} + \frac{1}{(A+B)^{\frac{3}{2}}}\right)^{\frac{1}{12}}, \quad (7)$$

$$A = \left(2.475\, ln\left(\frac{1}{\left(\frac{7}{Re}\right)^{0.9} + \left(\frac{0.27\varepsilon}{D}\right)}\right)\right)^{16}, \quad (8)$$

$$B = \left(\frac{37530}{Re}\right)^{16}. \quad (9)$$

2.2 Momentum Pressure Drop

The flashing of two-phase geothermal fluid occurs due to the pressure drop. This phenomena causes a velocity and momentum flux change in the two-phase geothermal fluid. The momentum pressure drop equation with an additional flashing factor ($1-x^2$) was proposed by Mundakir (2001):

$$\Delta p_m = \frac{G^2 v_e (1-x^2) D}{L}, \quad (10)$$

where G and v_e are the mass flux and effective specific volume which can be expressed as:

$$G = \frac{\dot{m}}{A}, \tag{11}$$

$$v_e = (xv_G + K(1-x)v_L)\left(x + \frac{(1-x)(1+(K-1)^2\phi)}{K}\right) \tag{12}$$

For calculating (11) and (12), the following equations are used:

$$v_H = xv_G + (1-x)v_L, \tag{13}$$

$$K = \sqrt{\frac{v_H}{v_L}}, \tag{14}$$

$$\phi = \frac{1}{\left(\sqrt{\frac{v_G}{v_L}} - 1\right)}. \tag{15}$$

2.3 Sudden Contraction Pressure Drop

A correlation for two-phase pressure drop across sudden contraction in ducts was developed by Schmidt and Friedel (1997). The Schmidt and Friedel (1997) correlation was modified by adding a flashing factor $(1-x^2)$ and parameter $\frac{1}{\beta}$ to enhance the accuracy and applied to a geothermal two-phase fluid:

$$\Delta p_C = \left(\frac{\dot{m}^2}{2\rho_{TP}d^2}\right)\left((1-\sigma^2C_C^2) - 2C_C(1-C_C)\right)(1-x^2)\left(\frac{1}{\beta}\right) \tag{16}$$

where (σ) is the area ratio, (C_C) is the contraction coefficient and (β) is the diameter ratio:

$$\sigma = \frac{A_{orifice}}{A_{pipe}}, \tag{17}$$

$$C_C = 1 - \frac{1-\sigma}{2.08(1-\sigma) + 0.5371}, \tag{18}$$

$$\beta = \frac{d}{D} \tag{19}$$

Finally, the net pressure drop for two-phase geothermal applications with an orifice is the sum of all the three components:

$$\Delta p_{net} = (\Delta p_f)_{seg.1} + (\Delta p_m + \Delta p_C)_{seg.2} + (\Delta p_f)_{seg.3} \tag{20}$$

3. GOVERNING EQUATIONS

The most accurate correlation and widest fluid enthalpy range for a geothermal two-phase orifice plate (concentric sharp-edge type) was developed by Mubarok et al. (2017):

$$\dot{m} = \frac{\left(\left(\frac{p_1}{p_2}\right)^{D\sqrt{\frac{\Delta p}{D}}}\right)\left(\frac{\pi d^2}{4}\right)\left(\sqrt{2\Delta p}\right)(9.7\times10^5 h^{-1.72})}{\left(\sqrt{1-\beta^4}\right)} \tag{21}$$

The flow of two-phase geothermal fluids through an orifice plate is turbulent for a Reynolds number larger than 5,000 (Reader-Harris, 2015). To accommodate the turbulent flow, the governing equations for a turbulence model are considered. In this study, the shear-stress transport (SST) $k-\omega$ model was used (ANSYS, 2013).

4. CFD MODEL SETUP

The parameter inputs for the CFD simulations were taken from the field experimental data of four geothermal wells in Indonesia; UBL-K/3 (Ulubelu field,) SBY-3 (Sibayak field), LHD-37/2 (Lahendong field) and BDN-A/1 (Bukit Daun field). The CFD models for the concentric orifice were developed using the same CFD parameters setup for each. The results of the CFD models were validated using the field data. A typical two-phase orifice plate installation for the field is shown in Figure 2 and Table 1.

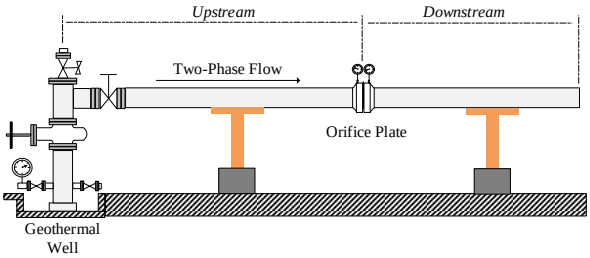

Figure 2: A typical two-phase orifice plate installation at a geothermal well.

The three-dimensional model was developed using ANSYS Design Modeler version 17 (ANSYS, 2013). The two-phase flow geometry was a segmented pipeline internal pipe diameter (D) and orifice diameter (d) which was located at the center (concentric type) and below the centerline of the pipe (eccentric type), as shown in Figure 3. The thickness of the plate (E) and the sharp-edge thickness (e) with bevel angle 45^0. The major axis of the pipe length was aligned with the (x)-axis of the domain.

The mesh for the flow solver simulation was created using ANSYS Meshing tools version 17. Unstructured triangular fluid domain meshes were created for the simulations with the minimum edge length for the tetrahedral cells of 3.2 mm. The mean values for the mesh skewness and aspect ratio were 0.23 and 4.82 respectively. A smooth transition of inflation layers was generated to increase the number of nodes near the surface with a transition ratio of 0.27, a maximum of 5 layers and a growth rate of 1.2.

Table 1: Operating Conditions and Geometry for Wells UBL-K/3, SBY-3, LHD-37/2 and BDN-A/1

Parameters	UBL-K/3	SBY-3	LHD-37/2	BDN-A/1	Unit
Geometry					
D	255	243	289	318	mm
d	170	170	202	222	mm
β (d/D)	0.7	0.7	0.7	0.7	
e	1.8	1.8	2.2	2.4	mm
E	5.2	5.2	6.1	6.7	mm
Taping distance	3,000	2,250	1,500	3,000	mm
Orifice plate type	Concentric sharp-edge				

Parameters	UBL-K/3	SBY-3	LHD-37/2	BDN-A/1	Unit
Operating conditions					
Fluid	Two-phase				
p_1	6.29	8.27	5.52	12.23	bara
	6.3E+05	8.3E+05	5.5E+05	1.2E+06	Pa
p_2	5.4	7.7	4.9	11.7	bara
	5.4E+05	7.7E+05	4.9E+05	1.2E+06	Pa
ΔP	0.8918	0.5307	0.6100	0.5099	bara
ρ_G	3.3	4.3	2.9	6.2	kg/m^3
ρ_L	906.8	895.6	911.7	877.4	kg/m^3
μ_G	1.4E-05	1.5E-05	1.4E-05	1.5E-05	kg/m.s
μ_L	1.7E-04	1.6E-04	1.7E-04	1.4E-04	kg/m.s
h	1,442	1,231	674	1,268	kJ/kg
m	30.0	32.7	59.8	73.2	kg/s
x	36.7	24.7	0.8	23.5	%
m_G	11.0	8.1	0.5	17.2	kg/s
m_L	19.0	24.6	59.3	56.0	kg/s

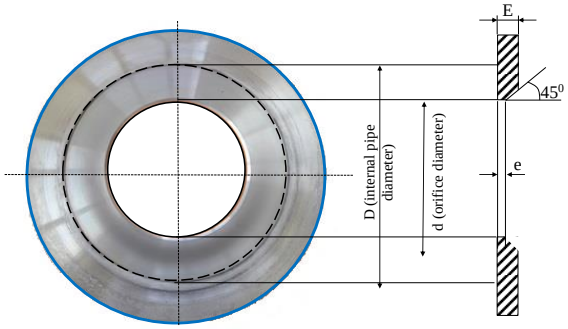

Figure 3: Cross-section of a concentric sharp-edge orifice plate (stainless steel).

To solve the Reynolds-Averaged Navier-Stokes (RANS) equations using ANSYS Fluent version 17, the following parameters were set:

1. Gravitational acceleration was set to -9.81 m/s^2.
2. The pressure (operating condition) and mass flow rate were set at the inlet and the no-slip condition was implemented on solid surfaces.
3. Water vapour was selected as the primary phase with density and dynamic viscosity.
4. The steady pressure-based solver, mixture model and the k-ω SST turbulence model were used.
5. The pressure-velocity coupling scheme was used with the maximum permissible Courant number set to 35.
6. Time step duration was 0.001s, a least squares cell-based and body-force upwind scheme were used for velocity gradients and pressure.
7. The first-order upwind scheme was chosen for momentum, volume fraction, turbulence kinetic energy and dissipation rate.
8. Standard initialization was used with an initial 27 m/s x-axis velocity.

A model verification study was completed using a Richardson Extrapolation technique to estimate the true solution (Shyy, Garbey, Appukuttan, & Wu, 2002). The extrapolated errors for different cases based on the predicted pressure drop (Δp) are shown in Table 2.

Table 2: Mesh Refinement Study

Parameters	Case 1	Case 2	Case 3	Case 4	Unit
Mesh Refinement					
Number of cells	186,688	419,825	959,423	2,156,968	
Volume	0.88				m^3
Mesh size	0.0168	0.0128	0.0097	0.0074	m
Mesh ratio	-	1.31	1.32	1.31	
Verification					
Δp from CFD	0.2025	0.2036	0.2043	0.2047	bar
Apparent order	1.43				
Richardson extrapolation	-	0.2004	0.2022	0.2033	bar
Extrapolated error	-	1.61	1.02	0.70	%

For the mesh refinement and numerical accuracy study in Table 1, all of the simulation models used the same mesh parameters with case 4 (2,156,968 elements).

The CFD models were successfully completed after the simulation was converged when the total continuity residual fell to < 10^{-5}.

5. RESULTS

The pressure drop prediction is calculated using the proposed analytical correlation (equation 20). For the validation, the results are compared to the field experimental data from UBL-K/3, SBY-3, LHD-37/2 and BDN-A/. The computed (CFD result) and calculated (using equation 20) net pressure drop for the two-phase geothermal fluid across the sharp-edge orifice plate (x-axis direction) is shown in Table 3. The predicted pressure drop (CFD and proposed correlation) was calculated from the different value of pressure of upstream (p_1) and downstream (p_2), while, a measured pressure drop (Δp) was obtained from field experimental data.

Table 3: Measured and predicted net pressure drop for UBL-K/3, SBY-3, LHD-37/2 and BDN-A/1

Parameter	UBL-K/3	SBY-3	LHD-37/2	BDN-A/1
Measured from Field Experiment				
Δp (bar)	0.8918	0.5307	0.6091	0.5099
Predicted from CFD Models				
Δp (bar)	0.8759	0.5381	0.5956	0.5058
Relative Error	1.78%	-1.39%	2.23%	0.82%
Predicted from Analytical Correlation (Eq. 20)				
Δp (bar)	0.8147	0.5161	0.5848	0.5311
Relative Error	8.64%	2.76%	4.00%	-4.15%

From Table 3, the predicted net pressure drop has good agreement compared to the field experimental data; it varies between -1.39% and 2.23% for the CFD result and from -

4.15% to 8.64% for the proposed correlation (equation 20). Therefore, both CFD models and proposed correlation (equation 20) can be used to predict the net pressure drop of geothermal two-phase fluid through a concentric orifice plate.

A comparison between calculated (equation 20), measured (Table 3) and CFD modeled pressure profiles through an orifice plate for geothermal two-phase flow in well UBL-K/3 is shown in Figure 4.

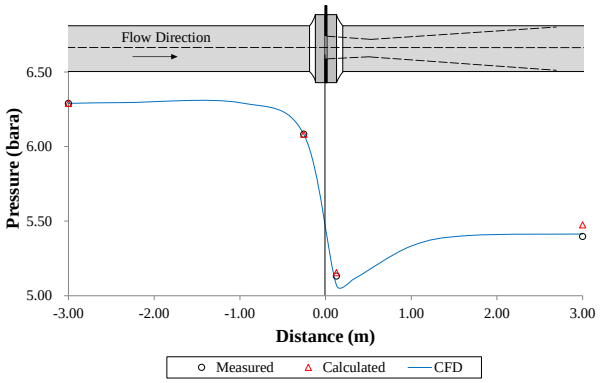

Figure 4: A comparison of pressure profiles through an orifice plate of well UBL-K/3 for the measured, calculated and CFD modeled.

The turbulent flow for concentric orifices at several axial locations has been investigated. As seen in Figures 5 to 7, the turbulent flow at the outlet (x>2.00 m) is fully developed for wells UBL-K/3, SBY-3 and BDN-A/1. The fully developed condition is indicated by the similar velocity shape at inlet (line 1) and outlet (line 6) as stated in Figures 5 to 7. The non-fully developed turbulent flow only occurred in well LHD-37/2 (Figure 8) because the CFD model outlet is limited to only 2 m away from the orifice plate.

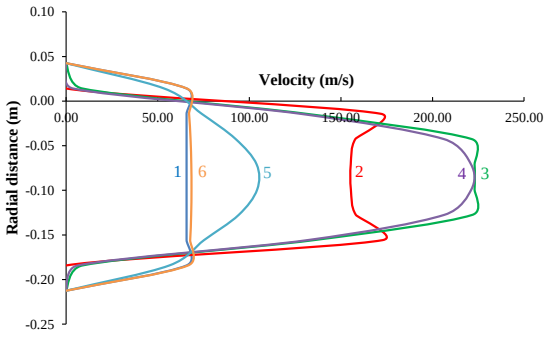

Figure 5: Computed axial velocity profile of well UBL-K/3 at various x-axis locations. (1) x=-3 m, (2) x=0 m, (3) x=0.1 m, (4) x=0.2 m, (5) x=1 m, (6) x=3 m.

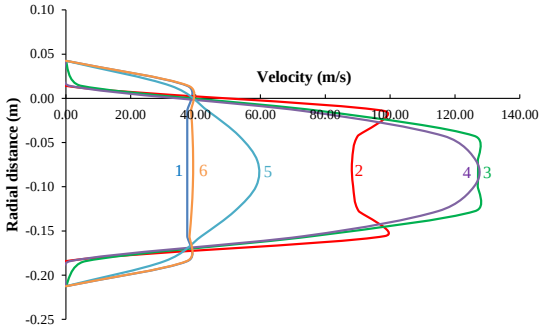

Figure 6: Computed axial velocity profile of well SBY-3 at various x-axis locations. (1) x=-2.5 m, (2) x=0 m, (3) x=0.1 m, (4) x=0.2 m, (5) x=1 m, (6) x=2.5 m.

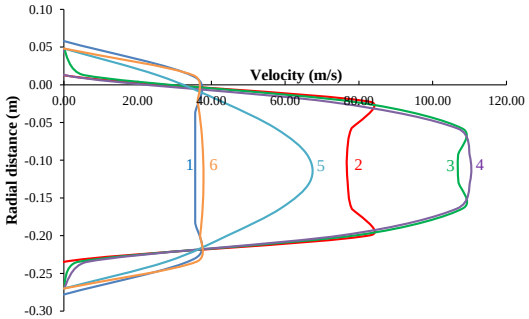

Figure 7: Computed axial velocity profile of well BDN-A/1 at various x-axis locations. (1) x=-3 m, (2) x=0 m, (3) x=0.1 m, (4) x=0.2 m, (5) x=1 m, (6) x=3 m.

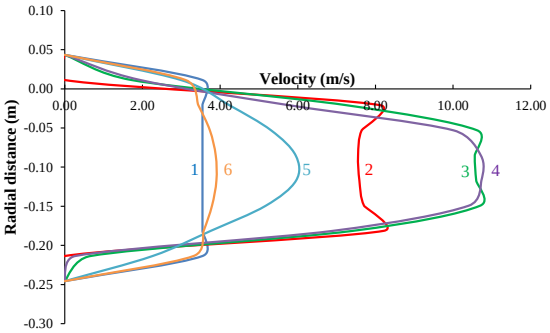

Figure 8: Computed axial velocity profile of well LHD-37/2 at various x-axis locations. (1) x=-2 m, (2) x=0 m, (3) x=0.1 m, (4) x=0.2 m, (5) x=1 m, (6) x=2 m.

Vertical cross sectional planes of pressure and three-dimensional velocity streamlines for UBL-K/3, SBY-3, LHD-37/2 and BDN-A/1 are shown in Figures 9 and Figure 10.

The highest velocity occurs at the orifice jet wall (approximately x=0.20 m) as shown in Figures 5, 6, 7, 8 and 10. This high velocity is caused by the flow separation process (Shah et al., 2012). The vena-contracta zone is visualized in the pressure contour (Figure 9) and the three-dimensional velocity (Figure 10). The vena-contracta zone is indicated by the separated flow at the top and bottom part of the pipe. The separated flow area at the pipe bottom part of the orifice plate occurs as shown in Figure 10. This indicates that there is a potential for scale deposition, which can decrease the orifice plate accuracy over time.

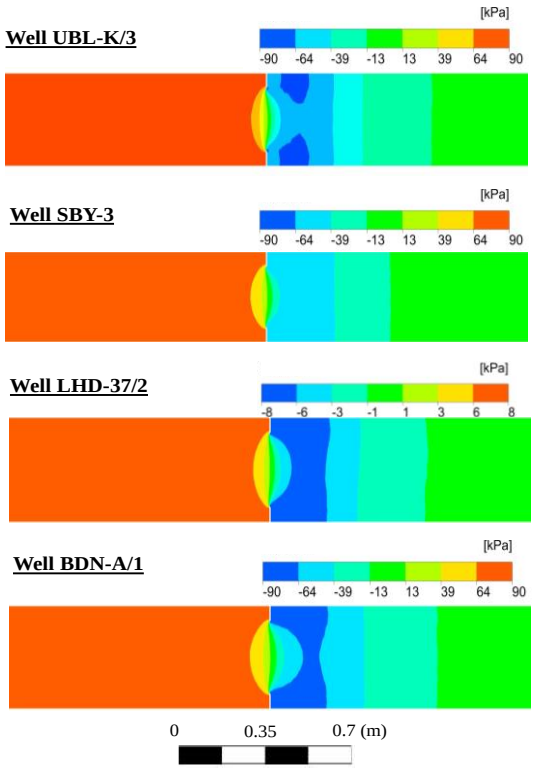

Figure 9: Pressure contours across the orifice plate for (a) UBL-(b) K/3 SBY-3, (c) LHD-37/2 and (d) BDN-A/1.

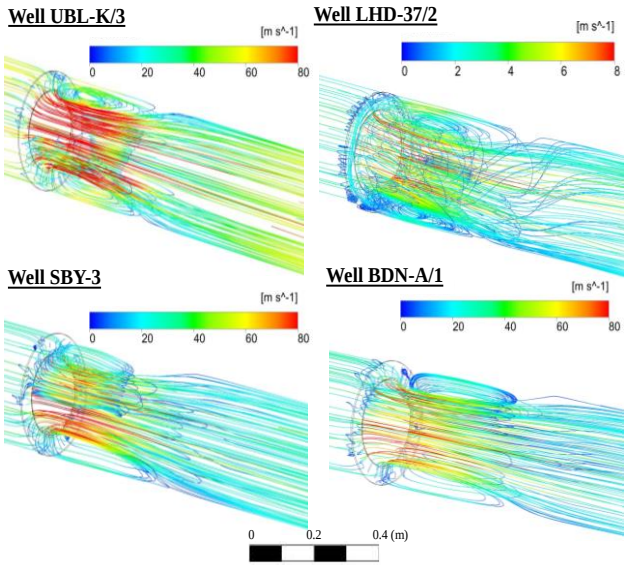

Figure 10: Three-dimensional steady state velocity streamlines across the orifice plate for UBL-K/3, SBY-3, LHD-37/2 and BDN-A/1 data.

The pressure drop at a radius tapping (D-D/2) type can be used to calculate the two-phase mass flow rate using the Mubarok et al. (2017) correlation. In this case, the pressure drop from the experimental data, CFD models and proposed correlation (equations 10 and 16) have been used to calculate the liquid (C_L) and steam discharge coefficients (C_G) and mass flow rate (Mubarok et al., 2017). Table 4 shows a comparison of the experimental data and simulated results. In general, both CFD models and proposed correlation (equations 10 and 16) are in good agreement when calculating the discharge coefficient. The relative error for discharge coefficient is less than 1% for all models. The predicted mass flow rates from the CFD models and analytical correlation (Eq. 20) have low relative error (**< 5 %**) compared to the field experiments data (Table 4).

Table 4: Discharge Coefficient and Mass Flow Rate Comparison

Parameter	UBL-K/3	SBY-3	LHD-37/2	BDN-A/1
Discharge Coefficient of Liquid, C_L				
Field Experiment	0.60640	0.60654	0.60677	0.60615
CFD Models	0.60642	0.60651	0.60677	0.60618
Analytical Correlation (Eq. 20)	0.60641	0.60653	0.60675	0.60617
Discharge Coefficient of Steam, C_G				
Field Experiment	0.60668	0.60683	0.60715	0.60635
CFD Models	0.60670	0.60680	0.60715	0.60639
Analytical Correlation (Eq. 20)	0.60669	0.60682	0.60713	0.60638
Mass Flow Rate (kg/s), Using Eq. 21				
Field Experiment	39.58	43.03	44.91	83.70
CFD Models	38.76	44.36	45.06	80.05
Relative Error	2.07%	-3.09%	-0.34%	4.36%
Analytical Correlation (Eq. 20)	39.10	43.45	45.88	81.30
Relative Error	1.22%	-0.98%	-2.15%	2.87%

6. CONCLUSIONS

An analytical correlation for the net pressure drop across a geothermal two-phase orifice plate has been developed based on the friction and momentum pressure drop with an additional empirical coefficient and flashing factor. The calculated net pressure drop and mass flow rate are compared to field experimental data for geothermal wells UBL-K/3, SBY-3, LHD-37/2 and BDN-A/1. The results show a good match with the relative error less than 9%.

Three-dimensional geothermal two-phase flow through the orifice plate has been simulated successfully using CFD using ANSYS-17.0. The results have good agreement compared to the field experiment data including pressure drop, discharge coefficient and mass flow rate. The proposed analytical correlation and the CFD model will be very useful for sizing the two-phase geothermal pipeline for each well and determine the appropriate orifice plate sizes and design.

ACKNOWLEDGMENTS

The author would like thank to PT. Pertamina Geothermal Energy (PGE), the University of Auckland (UoA) and New Zealand ASEAN Scholarship (NZAS) for the technical and financial support.

REFERENCES

ANSYS. (2013). *ANSYS Fluent theory guide*. Canonsburg: ANSYS, Inc.

Deendarlianto, Andrianto, M., Widyaparaga, A., Dinaryanto, O., Khasani, & Indarto. (2016). CFD Studies on the gas-liquid plug two-phase flow in a horizontal pipe. *Journal of Petroleum Science and Engineering*, 1-9.

Fadli, A. S., Karim, M. A., Harahap, R., & Taufik, A. (2015). *Pipeline failure analysis of bending pipe on the geothermal production well KMJ-X7 in Kamojang geothermal field, Indonesia*. Paper presented at the World Geothermal Congress 2015, Melbourne, Australia

Freeston, D. H. (1980). *A comparison of experimental result of pressure drop for two phase steam/water and air/water mixtures in a horizontal pipe*. Paper presented at the 7th Australasian Hydraulics and Fluid Mechanics Conference, Brisbane, Australia

Hollingshead, C. L. (2011). *Discharge coefficient performance of venturi, standard cocentric orifice plate, v-cone, and wedge flow meters at small Reynolds numbers.* (Master Thesis), Utah State University, Utah, USA. (869)

Jithish, K., & Kumar, P. A. (2015). Analysis of turbulent flow through an orifice meter using experimental and computational fluid dynamics simulation approach-A case study. *International Journal of Mechanical, 43*(4), 233-246.

Mazur, Z., Garcia-Illescas, R., & Porcayo-Calderon, J. (2009). Last stage blades failure analysis of a 28 MW geothermal turbine. *Engineering Failure Analysis, 16*, 1020-1032.

Mubarok, M. H., Zarrouk, S. J., & Cater, J. E. (2017). *The geothermal two-phase orifice plate*. Paper presented at the Proceedings 40th New Zealand Geothermal Workshop, Rotorua, New Zealand

Mundakir, A. (2001). *Geothermal two-phase pressure drop through a 90º elbow.* (Master of Engineering), The University of Auckland, Auckland, New Zealand.

Osato, K., Sato, M., & Kasai, K. (2016). *Coupled analysis using 3D-CFD and chemical model for corrosion and scaling of two-phase flow wellbore/pipeline.* Paper presented at the Proceedings 38th New Zealand Geothermal Workshop, Auckland, New Zealand.

Pointon, A. R., Mills, T. D., Seil, G. J., & Zhang, Q. (2009). *Computational fluid dynamic techniques for validating geothermal separator sizing*. Paper presented at the Geothermal Resource Council, Davis, USA

Purnanto, M. H., Zarrouk, S. J., & Cater, J. E. (2012). *CFD modelling of two-phase flow inside geothermal steam-water separators.* Paper presented at the New Zealand Geothermal Workshop Proceedings, Auckland, New Zealand.

Reader-Harris, M. (2015). *Orifice plates and venturi tubes*. In B. Wolfgang Merkirch, Germany, B. Donald Rockwell, USA & D. Cameron Tropea, Germany (Series Eds.). (pp. 393).

Roul, M. K., & Dash, S. K. (2012). Single phase and two-phase flow through thin and thick orifices in horizontal pipes. *Journal of Fluids Engineering, 134*, 1-14.

Schmidt, J., & Friedel, L. (1997). Two-phase pressure drop across sudden contactions in duct areas. *International Journal Multiphase Flow, 23*(1997), 283-299.

Shah, M. S., Joshi, J. B., Kalsi, A. S., Prasad, C. S. R., & Shukla, D. S. (2012). Analysis of flow through an orifice meter: CFD simulation. *Chemical Engineering Science, 71*, 300-309.

Shyy, W., Garbey, M., Appukuttan, A., & Wu, J. (2002). Evaluation of Richardson extrapolation in computational fluid dynamics. *Numerical Heat Transfer, 41*(B), 139-164.

Siba, M. A., Mahmood, W. M. F., Nuawi, M. Z., Rasani, R., & Nassir, M. H. (2015). Modeling and applications of 3D flow in orifice plate at low turbulent Reynold Numbers. *International Journal of Mechanical & Mechatronics Engineering, 15*(4), 19-25.

Urner, G. (1997). Pressure loss of orifice plates according to ISO 5167-1. *Flow Measurement and Instrumentation, 8*, 39-41.

Versteeg, H. K., & Malalasekera, W. (1995). *An introduction to computational fluid dynamics, The finite volume method*. England: Longman Group Ltd.

Zahariea, D. (2016). *Numerical analysis of eccentric orifice plate using ANSYS Fluent software*. Paper presented at the 20th Innovative Manufacturing Engineering and Energy Conference,

Zarrouk, S. J., & Purnanto, M. H. (2014). Geothermal steam-water separators: design overview. *Geothermics, 53*, 236-254.